DEPTH-DEPENDENCE OF MAGNETIZATION AT A FERROMAGNET EDGE UNDER THE INTERFACIAL DZYALOSHINSKII-MORIYA INTERACTION

DEPTH-DEPENDENCE OF MAGNETIZATION AT A FERROMAGNET EDGE UNDER THE INTERFACIAL DZYALOSHINSKII–MORIYA INTERACTION

Yuki Kaiya,[1] Syuta Honda,[1*] Hiroyoshi Itoh,[1] and Tomokatsu Ohsawa[2]

(Received November 12, 2021)

Abstract

The interfacial Dzyaloshinskii–Moriya interaction (I-DMI) occurs in a ferromagnetic wire on a heavy metal. Magnetic moments (MMs) at the edge of the wire are forcibly canted by the I-DMI. The influence of the canting MM at the wire edge on the wire interior is unclear. Here, we theoretically investigate the MMs under the I-DMI. The effect of the canting of MMs at the edge of the interior is shown to increase with a smaller exchange energy and a larger perpendicular anisotropy. A cosine of the cant angle of the MMs decreases exponentially with distance from the edge.

1 Introduction

Controlling the magnetic state of a ferromagnetic nanowire is necessary for the development of magnetic memories and arithmetic devices. A magnetic domain produced in the wire, which represents the binary digits of magnetic memories, is achieved by applying a spin current, or an external magnetic field.[1),2)] Spin-polarized current (SPC) induced domain motion is a particularly important issue for domain wall (i.e., racetrack) memories.[3)]

In a perpendicularly magnetized thin wire, a strip domain and a magnetic skyrmion are stabilized by the Dzyaloshinskii–Moriya interaction (DMI)[4)]. The interfacial DMI affects magnetic moments (MMs) near the interface and stabilizes the magnetic skyrmion, or strip domain, with a Néel-type domain wall in a wire layered upon a heavy metal, such as Pt or Ru.[5)]

In ferromagnetic wire on a heavy metal system, the magnetic states of the domain wall exert an influence on the domain motion.[6)] The domain wall length is calculated from the magnetic energy,[7)-9)] which is further discussed in Section 2. In a perpendicularly magnetized nanowire, the interfacial DMI strongly affects MMs near the wire edge and cants the MMs via a boundary condition of the magnetization at the edge.[10)]

As summarized above, the domain wall length and the MMs canting at the edge have been investigated in a perpendicularly magnetized wire under the interfacial DMI. When the width of the wire is narrower, the cant of the MMs affects the magnetization in the wire. Although

1 Department of Pure and Applied Physics, Kansai University, Suita, Osaka 564-8680, Japan
2 Department of Electrical and Electronics Engineering, National Institute of Technology, Numazu College, Numazu, Shizuoka 410-8501, Japan
* Correspondence to: Syuta Honda, Department of Pure and Applied Physics, Kansai University, Suita, Osaka 564-8680, Japan. E-mail: shonda@kansai-u.ac.jp

the behavior of the magnetization near the wire edge is important for designing a device with a narrower wire, the effects of the cant of the MMs at the wire edge on the magnetization inside the wire are unclear. Additionally, a long-range interaction is not included in the theoretical calculation of the magnetization at the wire edge although the magnetization direction depends on the position. The long-range interaction can be introduced in a micromagnetic simulation.

Using a one-dimensional model, we investigated the influence of canting MMs at the wire edge due to the interfacial DMI on MMs inside the wire without a magnetic domain. First, we analyzed, via theoretical calculation, the relationship between the depth-dependence of the canting MMs and the magnetic parameters, such as perpendicular anisotropy. Next, we compared our theoretically calculated results with those of a micromagnetic simulation. In Section 2, we introduce the theoretical analyses of the length of a domain wall, the edge canting MMs under the interfacial DMI, and the region length of canting MMs. In Section 3, the MMs of a one-dimensional wire with interfacial DMI are simulated using a micromagnetic approach. In Section 4, we discuss our results and then summarize our study in Section 5, the conclusion.

2 Theoretical analysis of the region length of canting MMs

2.1 Related work for the domain wall length

A domain wall length is estimated from an exchange energy and an anisotropic energy. Under a quasi-one-dimensional model, the exchange energy is given as

$$E_{\mathrm{ex}} \approx \int_{x_0}^{x_1} AS\left(\frac{\partial\theta}{\partial x}\right)^2 dx \tag{1}$$

and the anisotropic energy as

$$E_{\mathrm{k}} = S\int_{x_0}^{x_1} K\sin^2\theta dx\,, \tag{2}$$

where A represents the exchange stiffness constant; K is the effective perpendicularly anisotropy constant; S is the cross-sectional area of the region of MMs of θ, where θ is defined as the angle between an easy axis of magnetization and the MM; and x_0 and x_1 are the positions of domain wall edges. The effective perpendicularly anisotropy constant K is defined as $K=K_0-\frac{1}{2}N_{\mathrm{d}}\mu_0 M_{\mathrm{s}}^2$, where K_0 is the intrinsic anisotropy constant; M_{s} the saturation magnetization; N_{d} the demagnetizing factor; and μ_0 the magnetic constant. $\frac{1}{2}N_{\mathrm{d}}\mu_0 M_{\mathrm{s}}^2$ is the energy density of the demagnetizing field. When K_0 is larger than $\frac{1}{2}N_{\mathrm{d}}\mu_0 M_{\mathrm{s}}^2$, the magnetization points in the direction perpendicularly to the longitudinal direction of the wire.

$$\partial^2\theta/\partial x^2 = (K/A)\sin\theta\cos\theta \tag{3}$$

is given from $E_{\mathrm{ex}}+E_{\mathrm{k}}$ and the principle of least action.[7),8)]

Since θ of MMs changes from 0 rad to $-\pi$ rad at the domain wall,

$$\theta_{\mathrm{DW}}(x) = 2\arctan\left(\exp\left(-\frac{x}{\sqrt{A/K}}\right)\right) \tag{4}$$

is given from (3), where $x=0$ is the middle of the domain wall, which is plotted with a solid curve in Fig. 1(a). By using a linear approximation with a gradient of $\partial\theta_{\mathrm{DW}}(x)/\partial x|_{x=0}$, the length of the domain wall L_{DW} in a perpendicularly magnetized thin wire is given as

$$L_{\mathrm{DW}} = \pi\sqrt{\frac{A}{K}}\,. \tag{5}$$

The linearly approximated $\theta_{\mathrm{DW}}(x)$ is also plotted with a broken line in Fig. 1(a). The exchange length L_{ex} is defined as $L_{\mathrm{ex}} = (A/K)^{1/2}$.[9]

In a perpendicularly magnetized nanowire, the interfacial DMI strongly affects MMs near the wire edge and cants the MMs via a boundary condition of the magnetization at the edge, as shown in Fig. 1(c).[7] The boundary condition is described by the equation:[10]

$$\frac{d\boldsymbol{m}'}{dn} = \frac{D}{2A}(\boldsymbol{z}\times\boldsymbol{n})\times\boldsymbol{m}'\,, \tag{6}$$

where D represents the interfacial DMI parameter, $\boldsymbol{m}'$ the unit vector of the MM, $\boldsymbol{n}$ the normal vector at the wire surface, and $\boldsymbol{z}$ the unit vector of the $+z$-direction, which is the direction perpendicular to the magnetized nanowire from the heavy metal. $d\boldsymbol{m}'/d\boldsymbol{n}$ is the directional derivative of $\boldsymbol{m}'$ for the direction of $\boldsymbol{n}$. Equation (6) is derived from a variation in the magnetic energy. For example, the boundary condition for the $-x$-direction at the edge is $\partial\boldsymbol{m}'/\partial x = D/(2A)\,(m_z,\ 0,\ -m_x)$ and from (6), $\boldsymbol{m}' = (m_x, m_y, m_z)$, $\boldsymbol{n} = (-1, 0, 0)$, and $\boldsymbol{z} = (0, 0, 1)$. The angle between the z-axis and the MMs at the edge, θ_0, is given by

$$\sin\theta_0 = \pm\frac{D}{2A}\sqrt{\frac{A}{K}} \tag{7}$$

from the above boundary condition and (3).[10]

2.2 Region length of canting MMs

We analyzed the length of the region in which the MMs are canted by the interfacial DMI and its boundary condition L_{D}, which is shown in Fig. 1(c). From (3) and (7),

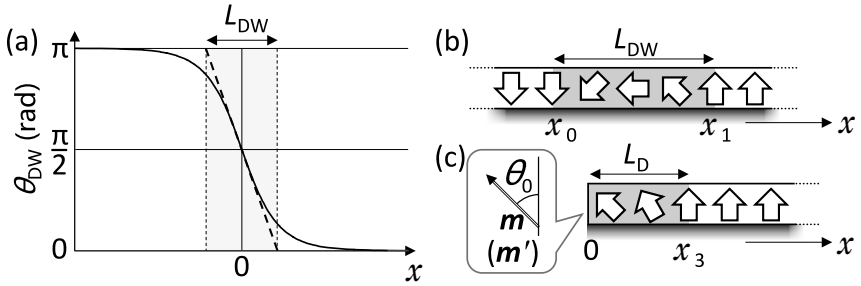

Fig. 1. Illustration of (a) θ_{DW}, (b) MMs near the domain wall, and (c) MMs by the edge in the nanowire under the interfacial DMI on heavy metal. Each thick arrow indicates the direction of the MM. The grey gradation regions in (b) and (c) represent the surface at which interfacial DMI occurs.

$$\theta(x) = 2\arctan\left(\tan\left(\frac{\theta_0}{2}\right) \exp\left(-\frac{x}{\sqrt{A/K}} \right) \right). \tag{8}$$

($\theta(x)$ with $\theta_0 = \pi/2$ equals to (4).) From a linear equation using $\partial\theta(x)/\partial x|_{x=0}$, L_D is calculated as

$$L_D = \frac{\theta_0}{\sin\theta_0}\sqrt{\frac{A}{K}}. \tag{9}$$

As L_D approaches $(A/K)^{1/2}$ and ∞, θ_0 approaches 0 and π, respectively. These convergence values are independent of the value of D.

We show $L_D(\theta_0)$ normalized by L_{ex} in Fig. 2. In our calculations, we presumed that θ_0 does not depend on A or K. Hence, it is presumed that θ_0, shown by a line in Fig. 2, changes as D changes.

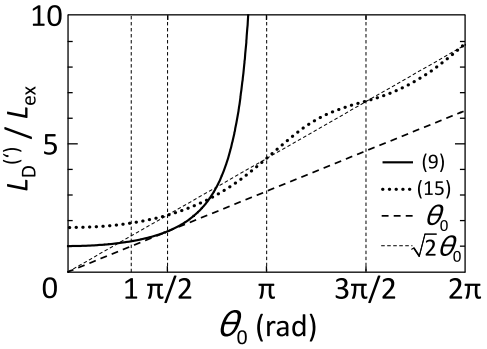

Fig. 2. L_D and L_D', which are estimated by Eq. (9) and (15), respectively, normalized by L_{ex}.

L_D / L_{ex} increases monotonically with increasing θ_0. L_D / L_{ex} touches the line of θ_0 at $\theta_0 = \pi/2$. At the other regions where $0 < \theta_0 < \pi/2$, L_D / L_{ex} is larger than the line of θ_0. $L_D(\theta_0 \geq \pi/2)$ is considerably increased with increasing θ_0.

3 Simulation of the magnetization

3.1 Model and method

Next, we show the simulation results of the magnetic structure in the wire with the interfacial DMI. In the simulation, the long-range dipole–dipole interactions, which are not considered in the aforementioned analysis, are taken into account in the calculations of the energy and the magnetic field. One-dimensional wire structures with 100 nm length in the x-direction ($l_x = 100$ nm, $l_y = 1$ nm, $l_z = 1$ nm) were used in the micromagnetic simulation. Simulations were carried out by dividing each wire into small cubic cells with dimensions of 1.0 nm × 1.0 nm × 1.0 nm, and the MM of each cell was calculated using the Landau–Lifshitz–Gilbert equation:[10),11)]

$$\frac{\partial \boldsymbol{m}}{\partial t} = -|\gamma|\,\boldsymbol{m}\times\boldsymbol{B}_{\text{eff}} + \alpha\,\boldsymbol{m}\times\frac{\partial \boldsymbol{m}}{\partial t}, \tag{10}$$

where $\boldsymbol{m}$ represents the unit vector of the MM within each cell; t the simulation time; γ =

-1.76×10^{11} rad·s^{-1}·T^{-1} the gyromagnetic ratio; and $\alpha=0.1$ the damping constant. $\boldsymbol{B}_{\mathrm{eff}}$ is the effective magnetic field composed of the contributions from long-range magnetic dipole–dipole interactions, short-range exchange interactions, interfacial DMI, and a perpendicular anisotropy term.

To estimate the effective magnetic fields, the following parameter values were set for the simulation: saturation magnetization $M_{\mathrm{s}}=1000$ kA·m^{-1}; $D=3.0$ mJ·m^{-2}; $A_0=15$ pJ·m^{-1}; and the intrinsic anisotropy constant $K_0=0.814$ MJ·m^{-3} ($K=0.50$ MJ·m^{-3}).[10] K was estimated from $K=K_0-\frac{1}{2}N_{\mathrm{d}}\mu_0 M_{\mathrm{s}}^2$, where $N_{\mathrm{d}}\sim0.5$ represents the demagnetizing factor; and μ_0 is the magnetic constant. The N_{d} is approximated by an infinite cylinder and $\frac{1}{2}N_{\mathrm{d}}\mu_0 M_{\mathrm{s}}^2$ is $\pi\times10^5$ J·m^{-3}. The K_0 value was chosen to move the effective perpendicular anisotropy constant of the simulation closer to that of previous analyses.

Since the magnetic characteristics of a wire are affected by the strength of the interfacial DMI and the magnetic properties of the wire, with the latter controllable by compositional and strain modulation,[12)-14)] in several simulations we used either $A'=\sigma A_0$ or $K_0'=\sigma' K_0$ instead of A_0 or K_0, respectively, to assess the relationship between the magnetization and the magnetic parameters. σ' provides $K'=\sigma K=\sigma' K_0-\frac{1}{2}N_{\mathrm{d}}\mu_0 M_{\mathrm{s}}^2>0$.

The boundary condition at the edge of the wire is $\partial\boldsymbol{m}/\partial x=D/(2A)\,(m_z,\ 0,\ -m_{\mathrm{x}})$. With one-dimensional systems, the boundary conditions at the longitudinal side edges are $\partial\boldsymbol{m}/\partial y=0$ and $\partial\boldsymbol{m}/\partial z=0$.

3.2 Simulation results

Two types of magnetizations were simulated to determine the effect of the boundary condition, represented in (6), on the magnetization. One is the magnetization considering the boundary condition of $d\boldsymbol{m}/dn=0$; and the other is that considering (6). The MM of each cell near the left edge is shown in Fig. 3.

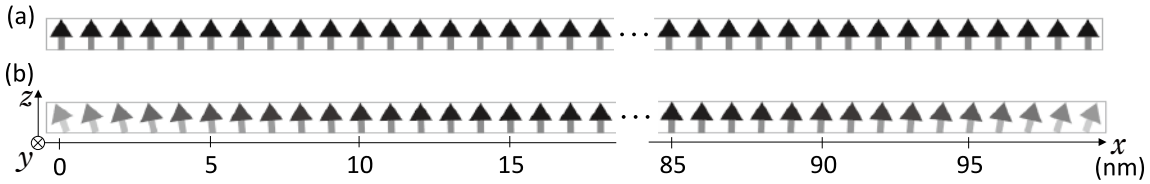

Fig. 3. Simulation results of the MMs in the one-dimensional wire considering the boundary condition of (a) $d\boldsymbol{m}/dn=0$ and (b) Eq. (6). The direction of the MM in each cell near the edge is shown with a small arrow.

The total magnetic energy of the system from (6) is 1.3×10^{-21} J smaller than that from $d\boldsymbol{m}/dn=0$. The following were considered: the energy difference of the magneto static energy from the long-range magnetic dipole–dipole interactions is -0.18×10^{-21} J; the exchange energy is $+0.49\times10^{-21}$ J; the perpendicular anisotropy energy is $+0.62\times10^{-21}$ J; and the interfacial DMI energy is -2.8×10^{-21} J. As the interfacial DMI decreases with consideration of the boundary condition of (6), the total energy decreases.

In the system with $d\boldsymbol{m}/dn=0$, all MMs pointed to the $+z$-direction, as shown in Fig. 3(a). Meanwhile, the MM at the edge ($x=1$ nm) canted outside of the wire in the system using (6), as shown in Fig. 3(b). The value of cant angle θ decreased with increasing x, and the MM canted slightly, even when $x=10$ nm.

When (6) boundary conditions are applied, the cant angle θ as a function of x is denoted by the open circles in Fig. 4. To consider the x-dependence of θ, we plotted $1-\cos\theta$ using a linear-log plot, as shown by the inset of Fig. 4.

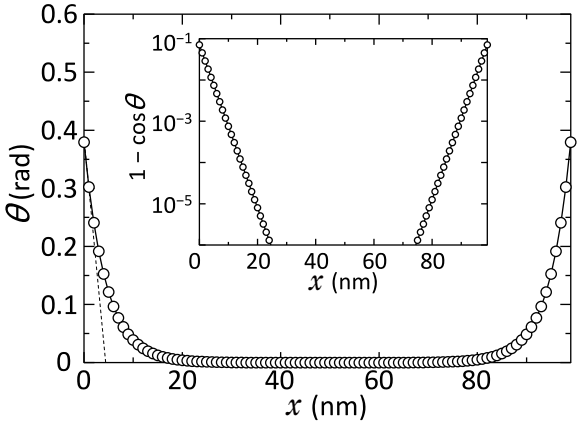

Fig. 4. Simulation results of the θ of each MM in the one-dimensional wire with Eq. (6). The inset shows the values that subtracted cos θ from 1 with a linear-log plot.

The simulated cant angle of MMs at the wire edges, θ_0, was 0.38 rad. This value is 33 percent smaller than $\theta_0 = 0.55$ rad, the analytical value. The simulated value of $\boldsymbol{m}$ at $x = 0$ nm was $(-\sin\theta_0, 0, \cos\theta_0)$ and $\boldsymbol{m}$ at $x = 1$ nm was $(-\sin\theta_1, 0, \cos\theta_1)$, where θ_1 was 0.30 rad. This variance is consistent with the analytical equation of the boundary condition.

The x-dependence of θ, $1-\cos\theta$, decreased exponentially as a function of x and its decay length was 2.2 nm. In other words, $1-\cos\theta$ can be approximated as $(1-\cos\theta_0)\ \exp(-x/\lambda)$ with $\lambda \approx 2.2$ nm.

Additionally, the above-simulated λ was compared with the analytical value. $\theta(x)$ of (8) is approximated as

$$1-\cos\theta(x) \approx \left(1-\cos\theta_0\right)\exp\left(-\frac{2}{\sqrt{A/K}}x\right). \tag{11}$$

$\frac{1}{2}(A/K)^{1/2}$ corresponds to λ and the analytical value of $\frac{1}{2}(A/K)^{1/2}$ is 2.7 nm, which is 23 percent greater than the 2.2 nm of λ estimated from the simulation.

We first estimated L_D using a linear approximation of θ from the simulation result. We plotted $f(x) = (\theta_1 - \theta_0)\ x\ /\ 10^{-9} + \theta_0$ in Fig. 4 (broken lines). x, provided $f(x) = 0$, is approximately 4.9 nm. We define x, provided $f(x) = 0$, as the L_D obtained from the simulation result. This value is 28 percent smaller than the analytical value of $L_D = 6.8$ nm calculated from (9) and using $\theta_0 = 0.38$ rad from the simulation result. This difference in the simulated and analytical values will be discussed in the next section.

Because several θ_0, λ, and L_D are discussed, we describe the two types of both θ_0, and λ, and the three types of L_D with the following notation and rule: $\theta_{0(a)}$ is calculated from (7); $\theta_{0(s)}$, $\lambda_{(s)}$, and $L_{D(s)}$ are obtained from the simulation result; $\lambda_{(a)}$ is calculated from $\frac{1}{2}(A/K)^{1/2}$; $L_{D(a)}$ is calculated from (7) and $\theta_{0(a)}$; and $L_{D(a,s)}$ is calculated from (9) and $\theta_{0(s)}$. For example, for the previously discussed cases, the simulated L_D of 4.9 nm is $L_{D(s)}$ and the analytical L_D of 6.8 nm, obtained from (9), is $L_{D(a,s)}$.

Next, we investigated the A-dependence of θ. Figure 5(a) shows θ of the MMs in the wire with an exchange stiffness constant of $A' = 0.5A_0 = 7.5$ pJ·m^{-1}, and $1.5A_0 = 22.5$ pJ·m^{-1}, in the closed triangles and closed squares, respectively. The wire with $0.5A_0$ had a $\theta_{0(s)}$ of 0.43 rad, which is larger than that in the wire with $1.0A_0$, where $\lambda_{(s)}$ and $L_{D(s)}$ were 1.3 nm and 3.2 nm, respectively. Meanwhile, in the wire with $1.5A_0$, $\theta_{0(s)}$, $\lambda_{(s)}$, and $L_{D(s)}$ were 0.34 rad, 2.9 nm, and 6.2 nm, respectively. The simulated A-dependence of $\theta_{0(s)}$, $\lambda_{(s)}$, and $L_{D(s)}$ showed the same behavior as the analysis results. These simulated values were also smaller than the values obtained in the analytical results.

Next, we investigated the relationship between K and θ. In Fig. 5(b), θ of the MMs in the wire with a perpendicular anisotropy constant of $K' = 0.5K = 0.25$ MJ·m^{-3} ($K_0' = 0.564$ MJ·m^{-3}) and $1.5K = 0.75$ MJ·m^{-3} ($K_0' = 0.106$ MJ·m^{-3}), is shown by the open triangles and open squares, respectively. All other magnetic parameters are the same as those described in Section 3.1, and the plot with the open circles in Fig. 5 is the same as that shown in Fig. 4.

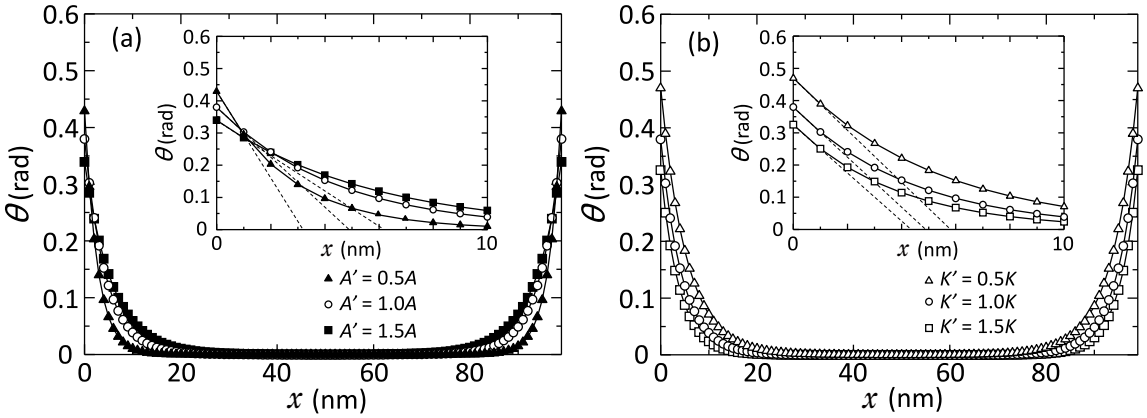

Fig. 5. Simulation results for θ of each MM in the wire with (a) $A'=A$ (circles), $0.5A$ (triangles), and $1.5A$ (squares) and (b) $K'=K$ (circles), $0.5K$ (triangles), and $1.5K$ (squares). A' and K' are the exchange stiffness constant and perpendicular anisotropy constant used in each simulation, respectively.

The wire with $0.5K$ had a $\theta_{0(s)}$ of 0.47 rad, which is larger than that in the wire with $1.0K$. $\lambda_{(s)}$ and $L_{D(s)}$ were 2.7 nm and 5.9 nm, respectively. Meanwhile, when the wire had a value of $1.5K$, $\theta_{0(s)}$, $\lambda_{(s)}$, and $L_{D(s)}$ were 0.33 rad, 1.9 nm, and 4.3 nm, respectively. The behavior of the simulated K-dependence of $\theta_{0(s)}$, $\lambda_{(s)}$, and $L_{D(s)}$ is consistent with that of the analytical results. However, these simulated values are lower in magnitude than the analytical results.

Each simulation value and analytical value is described in Fig. 6. Although we can represent the two curves as a function of $\sigma D^2/AK$, they are shown to clarify the A-, K-dependence of λ and L_D.

Figure 6(a) compares $\theta_{0(a)}$ and $\theta_{0(s)}$. The minimum value of σ in the analysis is 0.3. $\theta_{0(a)}$ approaches $\pi/2$, as σ approaches 0.3. $\theta_{0(s)}$ in the wire, with $\sigma > 0.3$, $\theta_{0(s)}$ decreased with increasing σA. This behavior is consistent with $\theta_{0(a)}$. When $\sigma < 0.3$, the value of $\theta_{0(s)}$ increased with decreasing σA. Meanwhile, $\theta_{0(s)}$ monotonically decreased with increasing σK. Comparing $\theta_{0(s)}$ and $\theta_{0(a)}$ in the wire, with $\sigma < 0.3$, is challenging. The difference between the A- and K-dependence of $\theta_{0(s)}$ is a result of long-range magnetic dipole–dipole interactions and the fact that this is a one-dimensional system. The $\theta_{0(s)}$ values were smaller than $\theta_{0(a)}$ values. These

differences will be discussed in Section 4.

Figure 6(b) shows the comparison between $\lambda_{(a)}$ and $\lambda_{(s)}$. We estimated that $\lambda_{(s)}$, from θ, to be in the range of $0 < x < 10$ nm. Although the characteristics of A- and K-dependence of $\lambda_{(s)}$ were consistent with that of $\lambda_{(a)}$, these simulation values were also smaller than those of the analytical results.

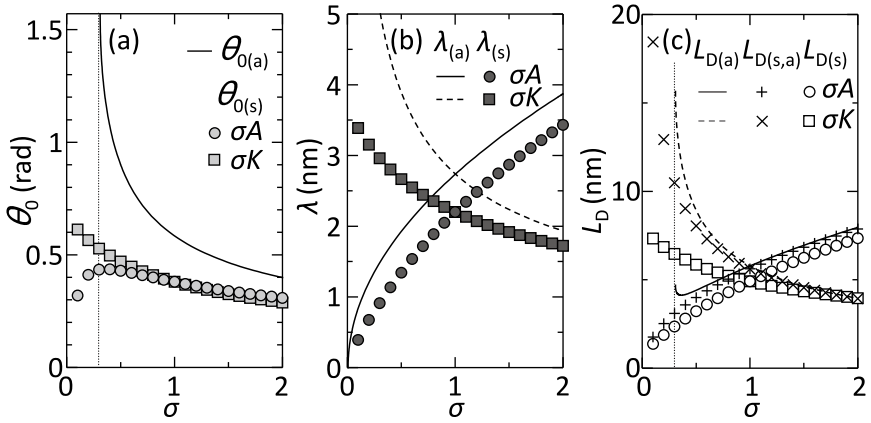

Fig. 6. A- and K-dependence of (a) θ_0, (b) λ, and (c) L_D. σA_0 or σK_0 instead of A or K, respectively. (a) The solid curve indicates the A- and K-dependence of $\theta_{0(a)}$. The circles and squares indicate the A- and K-dependence of $\theta_{0(s)}$, respectively. (b) The solid and dashed curves indicate the A- and K-dependence of $\lambda_{(a)}$, respectively, and the circles and square indicate the A- and K-dependence of $\lambda_{(s)}$. (c) The solid curve, open circles, and plus signs indicate the A-dependence of $L_{D(a)}$, $L_{D(a,s)}$, and $L_{D(s)}$, respectively, and the dashed curve, open squares, and cross marks indicate the K-dependence of $L_{D(a)}$, $L_{D(a,s)}$, and $L_{D(s)}$, respectively.

The comparison of three types of L_D is shown in Fig. 6(c). The A-dependence of $L_{D(a,s)}$ was closer to that of $L_{D(a)}$. From Fig. 2, we observed that the θ_0-dependence of L_D is small when θ_0 is smaller than 1 rad. Hence, the A- and K-dependence of $L_{D(a,s)}$ is almost equal to that of $L_{D(a)}$, although the A- and K-dependence of $\theta_{0(s)}$ differs from that of $\theta_{0(a)}$. However, the A- and K-dependences of $L_{D(s)}$ were smaller than those of $L_{D(a)}$ and $L_{D(a,s)}$. Almost all $\theta_{0(s)}$, $\lambda_{(s)}$, and $L_{D(s)}$ values were smaller than the analytical values, as will be discussed later.

In our system thus far, MMs at the edges cant outside of the edge. When D is -3.0 mJ·m^{-2}, MMs at the edges cant inside the edge, as shown in Fig. 7, and θ_0 was 0.53 rad.

Fig. 7. Simulation results of MMs in the one-dimensional wire with $D = -3.0 \times 10^{-3}$ J·m^{-2}. The direction of MMs near the edges is indicated with arrows.

4 Discussion

One reason for the difference between simulation and analytical results is the estimation and presumption of demagnetization. The anisotropy energy, (2), considers the local dipole interaction but not the long-range magnetic dipole–dipole interactions. To estimate the K_0

used in the simulation, we assumed a demagnetizing factor of an infinite cylinder; however, our focus is on the magnetization near the edge. When the magnetization cants at the edge, a magnetic pole is produced there. At the edge of the wire, having the equable MMs, N_d for $\frac{1}{2}N_d$ $\mu_0 M_s^2$ is 0.2 (diagonal elements of the demagnetizing tensor are $N_x=0.2$, $N_y=0.4$, $N_z=0.4$). Furthermore, in the wire with position-dependent MMs, the demagnetizing factor decreases further and the K_0 approaches K nearer the edge, assuming K is independent of position. The position-dependence of K_0 may influence the results of the study.

In this study, the values of the minimum $L_{D(a)}=(1.5A/K)^{1/2}$ and $\lambda_{(a)}=\frac{1}{2}(A/K)^{1/2}$ are approximately 6.71 nm and 2.8 nm, respectively, with 15 pJ·m^{-1} of A and 0.50 MJ·m^{-3} of K. For comparison, we have calculated $L_{D(a)}$ and $\lambda_{(a)}$ for other perpendicularly magnetized materials. CoFeB has an A value of approximately 30 pJ·m^{-1} and $K=0.50$ MJ·m^{-3}.[15),16)] In this case, the minimum $L_{D(a)}$ and $\lambda_{(a)}$ are approximately 9.5 nm and 3.8 nm, respectively. TbFeCo has an A value of approximately 1.0 pJ·m^{-1} and $K=0.1$ MJ·m^{-3},[17)] resulting in a minimum $L_{D(a)}$ and $\lambda_{(a)}$ of approximately 3.9 nm and 1.6 nm, respectively. Based on their A and K values, better-known perpendicular magnetized materials may have $L_{d(a)}$ and $\lambda_{(a)}$ values of several dozen nanometers.

The value of intrinsic anisotropy K_0 was approximately 60 percent larger than that of effective anisotropy K in our findings. This resulted in the difference between the analytical and simulation results. Some materials might have a K that is close to K_0. It is known that the saturation magnetization of TbFeCo can be controlled from 45 kA/m to 350 kA/m with a compositional modulation[17)]. In the case of $M_s=45$ kA/m, the demagnetization energy density, $\frac{1}{2}\mu_0 M_s^2$, is 1.27 kJ·m^{-3}, which is sufficiently smaller than the 0.1 MJ·m^{-3} of the effective anisotropy energy density, which we assume to be the maximum value of N_d. The demagnetization hardly depends on the effective anisotropy, and hence the K_0 value approaches the K value. In this case, the simulation results may equal the analytical results.

Earlier, we estimated L_{DW} by using the linear approximation with a gradient of $\partial\theta(x)/\partial x|_{x=0}$. The domain wall length is sometimes estimated using a different approximation.[8)] In such a case, $\theta(x)$ is approximated as a linear equation prior to the energy calculation. In the DW, $\theta(x)$ in the integrand for the energy calculation is approximated as $\theta(x)=(\pi/L_{DW})x$ because $\theta(x)$ changes from 0 to π rad by L_{DW}. Hence, this anisotropic energy E_k' is approximated as

$$E_k' \approx \frac{SL_{DW}'}{\pi}\int_0^{\pi} K\sin^2\theta d\theta\,, \tag{12}$$

and the domain wall length L_{DW}' is also given as

$$L_{DW}' = \sqrt{2}\pi\sqrt{\frac{A}{K}} \tag{13}$$

from $\partial(E_k'+E_{ex})/\partial L_{DW}=0$ of the variation principle.

Similarly, L_D is also calculated. In the integrand for the energy calculation $\theta(x)$ is approximated as $\theta(x)=-(\theta_0/L_D')x+\theta_0$. Here, we express L_D' and E_k'' as L_D and E_k, respectively. E_k'' for L_D' is approximated as

$$E_k'' = \frac{SL_D'}{\theta_0}\int_0^{\theta_0} K\sin^2\theta d\theta\,, \tag{14}$$

and L'_{D} is given as

$$L'_{\mathrm{D}} = \sqrt{2}\theta_0 \sqrt{\frac{A}{K\left(1-\dfrac{\sin 2\theta_0}{2\theta_0}\right)}}\,. \tag{15}$$

L'_{D} is normalized by L_{ex}, as shown by the dotted curve in Fig. 2. L'_{D} increases with oscillation as θ_0 increases $L'_{\mathrm{D}}/\,L_{\mathrm{ex}}$ by $\theta_0 \geq \pi/2$ is near value to $\sqrt{2}\theta_0$. Meanwhile, $L'_{\mathrm{D}}/\,L_{\mathrm{ex}}$ by $\theta_0 < \pi/2$ fails to attain $\sqrt{2}\theta_0$ and L'_{D} by $\theta_0 = 0$ approaches to $\sqrt{3}\,L_{\mathrm{ex}}$.

A similar analysis applies to the system with a perpendicularly magnetized film or wire. For example, if θ is changed to θ_{a} from θ_{b}, E_{k} is substituted with

$$E'''_{\mathrm{k}} = \frac{SL_{\mathrm{W}}}{\theta_b - \theta_a}\int_{\theta_a}^{\theta_b} K\sin^2\theta d\theta\,, \tag{16}$$

and the domain wall length L_{W} is estimated as

$$L_{\mathrm{W}} = \sqrt{2}\left|\theta_b - \theta_a\right| \sqrt{\frac{A}{K\left|1-\dfrac{\sin 2\theta_b - \sin 2\theta_a}{2(\theta_b - \theta_a)}\right|}}\,. \tag{17}$$

This formula might apply to a domain wall formed at a corner in an L-shaped wire or a domain wall in a wire with magnetizations canting by application of an external magnetic field and a SOT.

5 Conclusion

The interfacial DMI exerts an influence over the MMs by the edges in the nanowire. The magnitude and the effects of canting MMs inside the wire depend on A, K, and D values. The L_{D} is approximately $(A/K)^{1/2}$ when θ_0 is small. The x-dependence, $1-\cos\theta(x)$, decreases exponentially with $\frac{1}{2}(A/K)^{1/2}$ of its decay length (the inset of Fig. 4 and (11)). The effect of canting of the MM at the edge on the inside grows with smaller A and larger K values. The length of the canting MM is approximately ten nanometers in better-known perpendicularly magnetized materials. This canting might have some effect on the domain formed in a narrow width wire. Our results are useful for magnetization analysis in magnetic devices with a ferromagnet layered on a heavy metal, such as domain motion memories and magnetic random access memory. Our studies use a one-dimensional model without the magnetic domain. Future studies should investigate the magnetic states of two- and three-dimensional models, such as a nanowire with the domain.

Acknowledgment

We are grateful to the Kansai University Fund for Supporting Young Scholars 2019.

References

1) A. Yamaguchi, T. Ono, S. Nasu, K. Miyake, K. Mibu, and T. Shinjo, Real-Space Observation of Current-Driven Domain Wall Motion in Submicron Magnetic Wires, *Physical Review Letter*, **92**, 077205 (2004).
2) T. Ono, H. Miyajima, K. Shigeto, K. Mibu, N. Hosoito, and T. Shinjo, Propagation of a Magnetic Domain Wall in a Submicrometer Magnetic Wire, *Science*, **284**, 468-470 (1999).
3) S. S. P. Parkin, M. Hayashi, and L. Thoms, Magnetic Domain-Wall Racetrack Memory, *Science*, **320**, 190-194 (2008).
4) J. Iwasaki, M. Mochizuki, and N. Nagaosa, Current-Induced Skyrmion Dynamics in Constricted Geometries, *Nature Nanotech.*, **8**, 742-747 (2013).
5) R. Tomasello, E. Martinez, R. Zivieri, L. Torres, M. Carpentieri, and G. Finocchio, A Strategy for the Design of Skyrmion Racetrack Memories, *Sci. Rep.*, **4**, 6784 (2014).
6) A. V. Khvalkovskiy, V. Cros, D. Apalkov, V. Nikitin, M. Krounbi, K. A. Zvezdin, A. Anane, J. Grollier, and A. Fert, Matching Domain-Wall Configuration and Spin-Orbit Torques for Efficient Domain-Wall Motion, *Phys. Rev. B*, **87**, 020402(R) (2013).
7) A. Hubert and R. Schaefer, Magnetic Domains: The Analysis of Magnetic Microstructures, *Springer*, (1998).
8) S. Blundell, Magnetism in Condensed Matter (Oxford Master Series in Physics), *Oxford Univ Pr*, (2001).
9) G. S. Abo, Y-Ki Hong, J. Park, J. Lee, W. Lee, and B.-C. Choi, Definition of Magnetic Exchange Length, *IEEE Trans. Magn.*, **49**, 4937-4939 (2013).
10) S. Rohart and T. Thiaville, Skyrmion Confinement in Ultrathin Film Nanostructures in the Presence of Dzyaloshinskii-Moriya Interaction, *Phys. Rev. B*, **88**, 184422 (2013).
11) Y. Nakatani, Y. Uesaka, and N. Hayashi, Direct Solution of the Landau-Lifshitz-Gilbert Equation for Micromagnetics, *Jpn. J. Appl. Phys.*, **28**, 2485 (1989).
12) G. Yu, Z. Wang, M. A.-Beygi1, C. He, X. Li, K. L. Wong, P. Nordeen, H. Wu, G. P. Carman, X. Han, I. A. Alhomoudi, P. K. Amiri, and K. L. Wang, Strain-induced Modulation of Perpendicular Magnetic Anisotropy in Ta/Cofeb/Mgo Structures Investigated by Ferromagnetic Resonance, *Appl. Phys. Lett.*, **106**, 072402 (2015).
13) M. D. Stiles, W. M. Saslow, M. J. Donahue, and A. Zangwill, Adiabatic Domain Wall Motion and Landau-Lifshitz Damping, *Phys. Rev. B*, **75**, 214423 (2007).
14) Y. Ren, Y. L. Zuo, M. S. Si, Z. Z. Zhang, Q. Y. Jin, and S. M. Zhou, Correlation Between Ultrafast Demagnetization Process and Gilbert Damping in Amorphous TbFeCo Films, *IEEE Trans. Magn.*, **49**, 3159-3162 (2013).
15) V. B. Naik, H. Meng, and R. Sbiaa, Thick CoFeB with Perpendicular Magnetic Anisotropy in Cofeb-Mgo Based Magnetic Tunnel Junction, *AIP Advances*, **2**, 04282 (2012).
16) C. Bilzer, T. Devolder, J.-V. Kim, G. Counil, C. Chappert, S. Cardoso, and P. P. Freitas, Study of the Dynamic Magnetic Properties of Soft Cofeb Films, *J. Appl. Phys.*, **100**, 053903 (2006).
17) M. T. Rahman, X. Liu, M. Matsumoto, and A. Morisako, Compositional Dependence Of

Magnetoresistance in Tbfeco Amorphous Film, *IEEE Trans. Magn.*, **41**, 2568-2570 (2005).